# Enhanced Crystallinity of Polymer Nanofibers without Loss of Nanofibrous Morphology via Heterogeneous Photothermal Annealing

Vidya Viswanath,[†] Somsubhra Maity,[‡] Jason R. Bochinski,[‡] Laura I. Clarke,*[,‡] and Russell E. Gorga*[,†]

[†]Fiber and Polymer Science Program and [‡]Department of Physics, North Carolina State University, Raleigh, North Carolina 27695, United States

S *Supporting Information*

ABSTRACT: Poly(ethylene oxide) electrospun nanofibers with a low concentration of embedded gold nanoparticles (AuNP) were subjected to postfabrication annealing via photothermal heating from the nanoparticles. The results, including nanofibrous mat morphology, crystallinity fraction as a function of annealing time and modality, and average crystallite size, were compared with that for conventional heating at the same average temperature. Maximum crystallinity is achieved more quickly under photothermal heating, and higher maximum crystallinity values, approaching the theoretical maxima for an entangled polymer (∼80%), are obtained. Photothermal heating better preserves the unique nanostructured morphology of the nanofibrous mat whereas significant fiber thickening and loss of porosity occur under conventional annealing treatment. With photothermal heating, heat may be predominantly applied within amorphous material within the fiber, which provides energy for the amorphous chains to reorient and then possibly crystallize but while preserving existing crystalline regions as well as the temperature-fragile nanofiber surface. This occurs because nanoparticles are spontaneously segregated within amorphous material due to their characteristic size. In the complex environment of a polymeric nanofiber where crystalline, aligned amorphous, and random amorphous material are all present, further spontaneous segregation of the AuNP to the random amorphous material may occur which enables targeting of this higher barrier to crystallization population, leading to very high final crystallinity fractions.
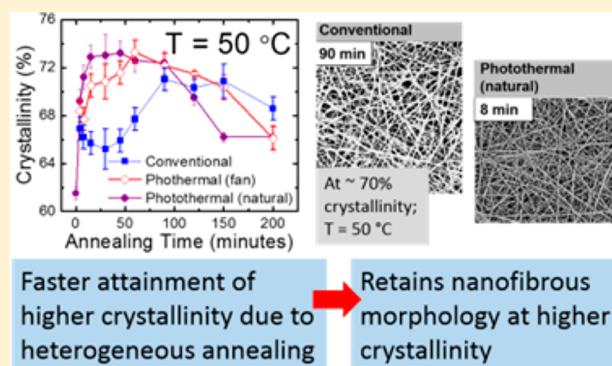
1. INTRODUCTION

Polymeric nanofibers are technologically useful low-cost, high surface area materials for applications such as tissue engineering,[1−3] drug delivery,[4,5] filtration,[6,7] and energy storage.[8,9] A common technique for generation of polymeric nanofibrous materials is electrospinning.[10] Nanofibers fabricated from electrospinning often have limited crystallinity as a result of the rapid loss of solvent and solidification during the electrospinning process, which can result in mechanical weakness.[11−13] Ideally, with postprocessing, the crystalline fraction within electrospun materials could be controllably increased; however, such a process is only useful if it also preserves the nanofibrous morphology within an electrospun mat. One common strategy to improve crystallinity in a semicrystalline polymer is thermal annealing at temperatures between the glass transition (T_g) and melt (T_m) temperatures. Such postprocessing studies on electrospun nanofibers suggest increased crystallite size and larger, more organized crystals (as well as evidence that moderate annealing may improve mechanical properties due to the formation of fiber−fiber bonds).[11,14−17] Beyond improving mechanical properties, annealing to increase crystallinity serves as a prototypical

example of a barrier-limited process that can be driven by internal or external heating.

The ideal process of crystallinity maximization involves selective thermally induced crystallization of amorphous regions coupled with simultaneous retention of any pre-existing crystalline structure. The lower the heating temperature utilized, the longer the time needed to achieve maximum crystallinity; however, when annealing using temperatures closer to the polymer melt temperature, undesirable melting and recrystallization (i.e., loss of existing crystallites) effects become more dominant. Melting and recrystallization in an annealing experiment generally lead to a dramatic decrease in overall crystalline fraction. An additional complicating factor when annealing nanostructures is the large surface area to volume ratio, which results in strong surface melting effects, where the innately less stabilized surface melts (or, more generally, relaxes) at a lower temperature than the sample interior. Furthermore, in electrospun materials the polymer

chains tend to be aligned and elongated along the fiber axis. This unstable quasi-equilibrium can lead to dramatic relaxation (including mat shrinkage) upon heating.[18−22] These factors suggest that a heterogeneous temperature distribution where, for example, the interior of the fiber is much warmer than the exterior and/or the amorphous regions hotter than the crystalline volumes may be a highly beneficial approach to postprocess polymeric nanofibers, thus retaining the useful nanostructured morphology while simultaneously allowing relatively rapid improvement of the crystalline faction. Such an approach would be in sharp contrast to conventional heating (heat propagation from the outside in) where the surface is the first to warm, and the entire sample reaches a homogeneous temperature which can lead to both increased surface melting and loss of existing crystalline regions.

We explore the approach of creating a heterogeneous temperature distribution within polymer nanofibers by using a low concentration of gold nanoparticles (AuNP) as internal, optically controlled, nanoscale heat sources. The size scale of the nanoparticles (~20 nm diameter) indicates (from steric considerations) that they will be predominantly located within amorphous regions.[23] Metal nanoparticles exhibit a localized surface plasmon resonance (SPR) and generate thermal energy when incident light resonant with the SPR is absorbed and converted into heat.[24] Such photothermal heating has been previously demonstrated in aqueous systems,[25−32] as well as solid polymer environments such as films,[33−38] with a few reports within nanofibrous systems.[39−42] Because the heat is generated at the nanoparticles, these sites are the warmest points in the solid, and the steady-state temperature decreases moving away from such thermal hot spots.[43−50] In principle, this temperature difference provides rapid annealing in the amorphous regions while preserving the existing crystalline structure and the nanofibrous morphology of the surface.

Photothermal heating in a nanofibrous system (which has a high porosity, >70%) will differ from that in bulk materials as conduction along the very small cross-sectional area (typical diameter ~200 nm) fibers will be the predominant heat loss mechanism, in competition with natural convection losses through the air surrounding each fiber.[51,52] This heterogeneous environment is much more complex than the relatively homogeneous region surrounding a heated nanoparticle within a liquid or a bulk solid medium where primary heat loss by conduction occurs uniformly in all directions.[31,46,53] Moreover, the environment within an electrospun fiber is more complicated than in a polymer thin film, with areas dominated by elongated amorphous chains and other regions which are strongly entangled, in addition to the typically row-nucleated lamellar structures forming the crystalline portions. This morphology is quite different than the spherulitic structures observed in bulk semicrystalline polymers. In this report, we compare the effects of postfabrication annealing (including nanofibrous mat morphology, crystallinity fraction, and average crystallite size) in a metal (gold) nanoparticle: poly(ethylene oxide) (AuNP:PEO) electrospun nanofibrous composites via conventional means with that obtained from photothermal heating at the same average temperature.

2. EXPERIMENTAL SECTION

2.1. Metal Nanoparticle Synthesis. Frens' method was used to synthesize citrate-stabilized spherical gold nanoparticles[54] wherein aqueous tetrachloroauric(III) acid was reduced with aqueous trisodium citrate solution (both Sigma-Aldrich). Dry polyvinylpyrro-

lidone (PVP) (Scientific Polymers Products, Inc.) was added to the solution in an amount equal to that of the tetrachloroauric(III) acid to further stabilize the nanoparticles after synthesis. Characterization of gold nanoparticles utilized transmission electron microscopy (TEM) (Hitachi HF2000 transmission electron microscope) images of freshly prepared nanoparticle solution drop-cast directly onto copper grids (Ted Pella, PELCO 400 mesh grids) (see Supporting Information Figure S3). Spherical nanoparticles were observed to have an average diameter of 19 ± 3 nm. Extinction spectra of the solution were measured with an ultraviolet−visible spectrometer (CARY 50 Scan) identifying the peak of surface plasmon resonance (SPR) at 527 nm.

2.2. Nanocomposite Mat Fabrication. Poly(ethylene oxide) (PEO) (Scientific Polymer; molecular weight 400 000 g/mol) was added to the AuNP water-based solution along with perylene in powder form (Sigma-Aldrich # 394475-1G) obtain a 6 wt % solution, resulting in 0.25 wt % AuNP:PEO and 0.09 wt % perylene:PEO in the final solid nanofibrous sample after electrospinning. The solution was magnetically stirred for 24 h at room temperature before electrospinning.

The AuNP:PEO solution was electrospun using a traditional needle electrospinning set up with a 5 cm long, 18 gauge stainless steel needle. A programmable syringe pump (New Era Pump Systems, Model NE 500) extruded the solution from a 12 mL syringe and with a positive polarity high voltage applied to the needle (Glassman High Voltage, Model No. FC60R2). A feed rate of 4 μL/min with an operating voltage of 11 kV and working distance of 12 cm were used. The grounded collector was covered with aluminum foil to collect the randomly oriented nanofibrous mat. The nanofibrous samples were electrospun for 1 h to obtain mats with a thickness of 7 ± 3 μm as measured by an alpha step profilometer (VeecoDektak Model 150). The mats were subsequently annealed by conventional or photothermal heating at average temperatures ranging from 40 to 60 °C for 4−400 min.

2.3. Annealing Methods and Temperature Measurement. Three different methods of postprocess annealing were used to treat the nanofibrous samples: conventional annealing, photothermal annealing (natural-cooled), and photothermal annealing (fan-cooled). Conventional annealing of the nanofibrous samples was carried out using a temperature-controlled heated stage utilizing a copper block 2.5 cm × 7.5 cm × 1 cm attached to a commercial hot plate (VWR 7X7 CER hot plate), the details of which have been described previously.[38] The average temperature attained by the mat during initial heat-up, the active annealing time at a given annealing temperature, and the cooldown to room temperature were monitored via a fluorescence technique (described below). The heat-up profiles were matched so that the time to reach steady state was the same for each annealing modality.

For photothermal annealing, samples were mounted on the same stage at room temperature and irradiated with 514 nm light. In this work, light intensities (measured using a power meter (Coherent Model Powermax PM10)) ranging from 0.078 to 0.125 W/cm^2 were utilized, resulting in steady state temperatures of 40 ± 2.4 to 60 ± 1.8 °C. The average temperature of the system was increased by increasing the laser intensity, as discussed in detail previously.[38,55] Samples that experienced photothermal annealing cooled significantly slower than conventionally annealed samples after the removal of the heating source. This effect was observed to be most pronounced at higher annealing temperatures (60 °C) where photothermally annealed samples took almost 20 min longer than conventionally annealed samples to cool down to room temperature (i.e., ~40 min to cool as compared to ~23 min cooldown time in conventionally annealed samples). In order to isolate the effect of cooling from that of annealing temperature and duration alone, a third protocol was implemented wherein photothermally heated samples were actively fan-cooled. Thus, in the fan-cooled experiments, the cooling rate for photothermal annealing was matched to that observed under conventional annealing by the use of an external cooling fan such that the entire temperature cycle (i.e., heating, annealing, and cooling) was identical for the two types of thermal treatment.

A noncontact temperature measurement utilizing perylene as a fluorescent probe monitored the average temperature of the nanocomposite. Perylene displays temperature-dependent changes in its emission spectrum: in particular, the ratio of the emission intensity at the "trough" at 465 nm to that of the "peak" at 479 nm changes quasi-linearly, providing an in-situ probe of temperature.[42,55−57] The 514 nm emission was spectrally separated from the multiline output of an argon-ion laser (Coherent Sabre) using a dispersing prism, expanded to ∼3 cm $1/e^2$ diameter, and utilized as the photothermal heating beam. A 405 nm diode laser (∼5 mW), collimated to ∼5 mm $1/e^2$ diameter and amplitude-modulated at a 2 kHz rate using a flywheel chopper, was used to excite the perylene molecules. The two beams were spatially well-overlapped at the sample. Fluorescence from the excitation spot was imaged onto the front slit of dual-grating scanning spectrometer (SPEX 1680B); the instrument output is mated to a photomultiplier tube (PMT, Hamamatsu 931B). Dielectric filters on the input to the spectrometer (CVI) and the PMT (Omega Optical) were used to reject scattered laser light. The PMT output signal is amplified using a homemade instrument and photon-counted (SR400, Stanford Research Systems) with dark background corrected subtraction as the spectrometer iteratively samples the emission at the trough and peak wavelengths.

As previously discussed, perylene molecules are uniformly distributed throughout the entire sample, and thus the temperature measured via this technique is an average over all environments.[42] Because of the dilute doping of AuNP, the vast majority of perylene molecules (and, in fact, most of the polymeric sample) are relatively far from a gold nanoparticle. Thus, this temperature measurement provides a result which is slightly higher than, but very close to, the background temperature, which is the coolest temperature in the heterogeneously heated sample.[44,55,58]

2.4. Sample Characterization. Scanning electron microscopy (SEM) (JEOL JSM-6400 FE w/EDS, operating at 5 kV) images were used to study fiber morphology and porosity changes as a function of annealing conditions. Electrospun mats were sputter-coated with gold/palladium (∼10 nm) to reduce surface charging. Nanofiber diameters were obtained from an average of at least 100 points for each annealing condition from the SEM images using the NIH ImageJ software. Porosity of the electrospun webs was determined using ImageJ software, converting the SEM image to an 8 bit image, adjusting the pixel intensity to approximately select only the first layer of nanofibers and calculating this area fraction.[14,59] Porosity measurements from this image analysis method were consistent with direct density measurements (measuring the mass of a nanofibrous mat of known volume) where the literature values of PEO density and the law of mixing were used to estimate void space fraction.

Differential scanning calorimetry (DSC) (PerkinElmer Diamond DSC-7) was used to determine the crystalline fraction. Sample specimens were subjected to heating scans from 25 to 80 °C at a heating rate of 5 °C/min (first heating cycle). Pyris software was used to analyze the DSC data. Overall crystallinity (% X_c) was calculated from % $X_c = (\Delta H_m / \Delta H^*_m) \times 100$, where ΔH_m and ΔH^*_m are the melting enthalpies for the specimen and 100% crystalline PEO, respectively ($\Delta H^*_m = 213.7$ J/g).[60] No evidence of cold crystallization was observed. As fabricated, AuNP:PEO fibers showed a crystallinity fraction of ∼62.6 ± 1%, which is comparable with the value of 64.7 ± 1% in pure PEO nanofiber mats, indicating that addition of the metal nanoparticles neither enhanced nor limited the ability of the polymer to crystallize. Both as-fabricated as well as annealed samples (of all modalities, with and without nanoparticles) showed melt temperatures (T_m) between 65 and 68 °C.

To study annealing-induced crystal structure changes, wide-angle X-ray diffraction (WAXD) was performed at 2θ angles ranging between 5° and 30° using a step size of 0.01° on a Rigaku Smartlab diffractometer with Cu Kα radiation at a wavelength of 0.1541 nm. From the diffractograms, full width at half-maximum intensity (FWHM) and average crystallite size (calculated using the Scherer equation) are reported for the peak observed at 2θ angle ∼19.0° corresponding to the (120) reflection of PEO.[61]

3. RESULTS AND DISCUSSION

3.1. Increased Crystallinity without Compromising Nanofibrous Morphology. A key result in this study, demonstrated in Figure 1, is that photothermal annealing results in crystallinity increase without sacrificing the nanofibrous morphology of the nonwoven mat.

Figure 1a shows the crystallinity from DSC as a function of treatment time for each annealing modality. Each curve demonstrates the expected response: at first the crystallinity increases whereas at longer times, overt melting occurs which destroys existing crystallites, resulting in nonideal recrystalliza-
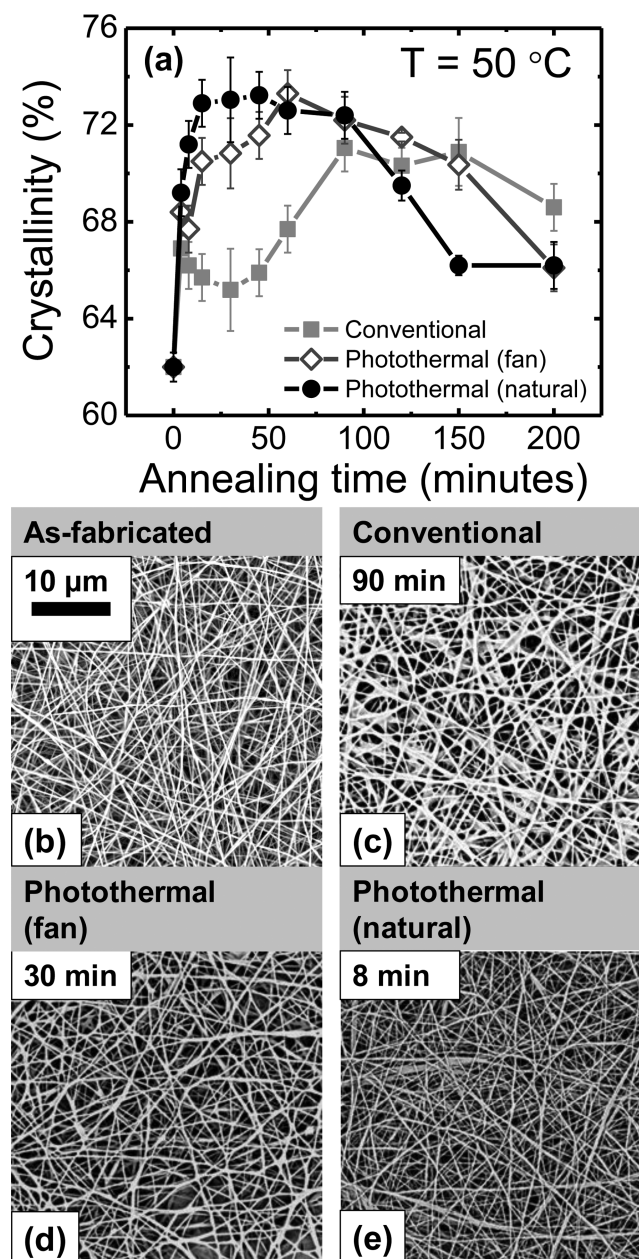

Figure 1. (a) Crystallinity as a function of annealing duration (minutes) at 50 °C (T_m − 15 °C). SEM images of (b) untreated AuNP:PEO nanofibers and samples at a 70% crystallinity which was achieved after annealing at 50 °C (c) for 90 min in a conventional oven, (d) for 30 min with photothermal annealing (fan cooling), and (e) for 8 min with photothermal annealing (natural cooling). The scale bar (shown in (b)) is the same for all images.

tion and thus a decreased crystalline fraction. Between these extremes, a maximum value is achieved. Here, the maximum crystallinity achieved under conventional annealing (filled square symbols in Figure 1a) is 70% which occurs at ~100 min. For the fan-cooled photothermal samples (with identical heating/cooling times to the conventional case, open diamond symbols) the maximum crystallinity is 73% which occurs at ~60 min. As discussed in greater detail previously,[37,38,42] the heterogeneous temperature distribution resulting from photo-thermal heating means that regions particularly close to the particles are significantly warmer than the average temperature in the sample. Thus, the effective dynamic temperature in the sample is higher under photothermal heating, which reduces the time needed to achieve maximum crystallinity. For the photothermal samples cooled naturally (slower cooling rate, closed circle symbols), the overall crystallinity was equal to that for the fan-cooled samples (73%) but occurred at ~20 min of active heating (vs 60 min). In this case (discussed further, in section 3.4), the sample remains warm after the SPR resonant light is removed, effectively increasing the annealing time as the sample slowly, naturally cools (i.e., the effective annealing time is longer).

Examining the morphology of the samples when reaching 70% crystallinity (Figure 1c–e) which occurs at different times for different protocols, we observe that the mat morphology is essentially completely preserved for the photothermal (natural cooling) case as confirmed by image analysis which shows the average fiber diameter (143 ± 32 nm) and porosity (76 ± 0.5%) are unchanged from that in the original, as-spun sample (Figure 1b, average fiber diameter 169 ± 27 nm, porosity 77 ± 0.4%). The photothermal samples that experienced fan cooling, which required a longer active treatment to achieve the same crystallinity level, have a morphology very similar to the original mats, with only a slight thickening of the fibers (204 ± 39 nm) and decreased porosity (73 ± 0.5%). In contrast, there is overt damage to the sample annealed under conventional conditions (average fiber diameter 350 ± 79 nm and porosity 61 ± 0.6%). This result highlights the utility of annealing with a heterogeneous heat profile. Under conventional conditions, the lower melting point surface of the sample is the first to warm as heat must penetrate through the fiber surface in order to reach the interior, causing surface relaxation and melting. In contrast, in the photothermal approach the fiber surface is the coolest region of the sample: heat is generated within the nanofiber, and the heat loss mechanism of convection and conduction by the air is the most dominant at the fiber surface. Thus, the fiber surface is less affected in the photothermal approach, leaving the nanostructured morphology intact.

Similar behavior was seen for samples at 60 °C ($T_m − 5$ °C, Figure 2, filled dark gray symbols) and 40 °C ($T_m − 25$ °C, Figure 2, filled black symbols). At all temperatures, the conventional annealing approach (Figure 2a) results in maximum crystallinity values ranging from 70 to 71%, which indicates that this is the highest achievable value under uniform heating at temperatures $T_m − 25$ °C to $T_m − 5$ °C. As discussed below (section 3.2), maximum crystallinity from photothermal approaches is always equal to or higher than the conventional result, reaching values as high as 78%. Comparing the morphology for samples with ~70% crystallinity (Table 1) (achieved for different times in different modalities) for 40 °C treatment, nanofiber diameter values after annealing overlap within error for all annealing modalities and are not significantly different from that within as-spun mats. Similarly,
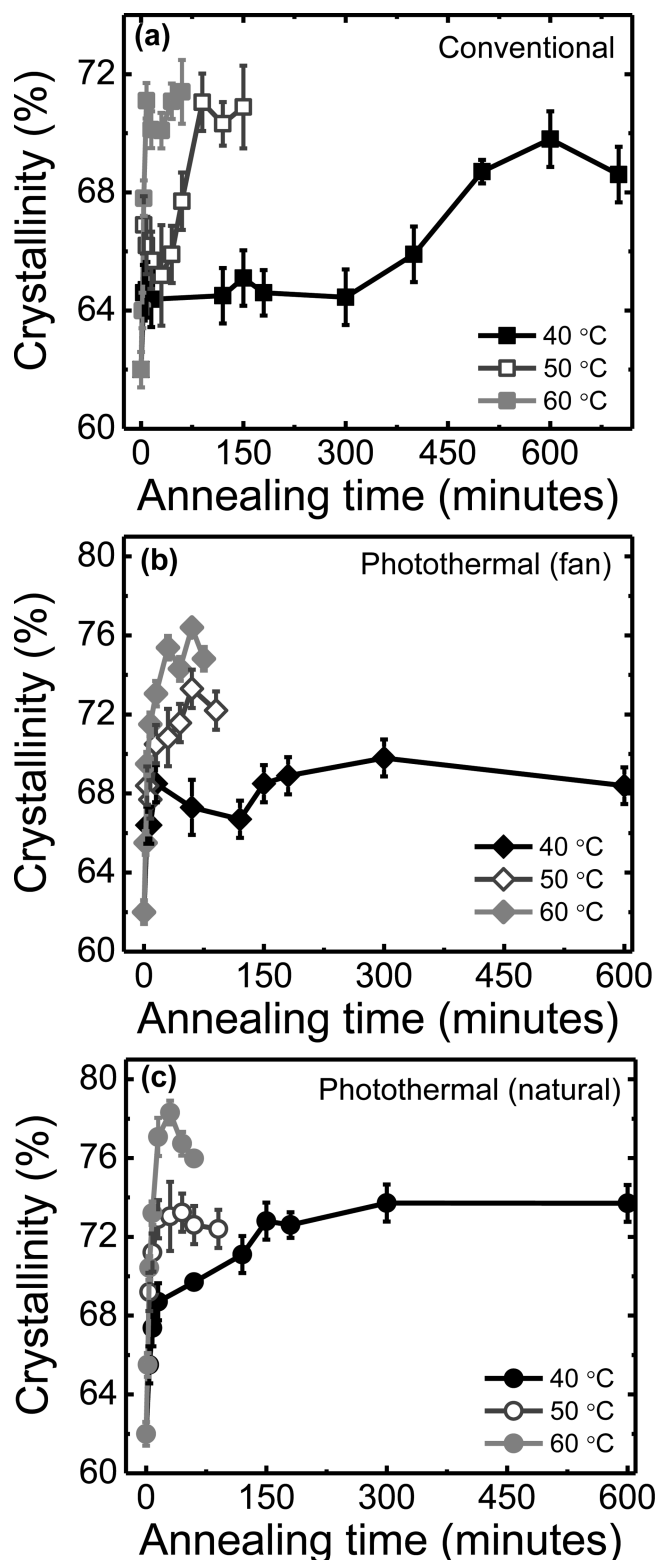

Figure 2. Crystallinity as a function of annealing duration (minutes) at various temperatures for (a) conventional or photothermal annealing (with (b) fan cooling or (c) natural cooling). Additional data in the recrystallization region (after the maximum value has been achieved) for the higher temperature data are not shown to ensure readability.

porosity values after annealing are also uniform across modalities with only small differences from the as-spun case. Here, the majority of the sample is always well below T_m, which

Table 1. Figure Diameter and Porosity from Analysis of SEM Images after Treatment at the Given Temperature in the Given Modality[a]

	diameter (nm)			porosity (%)		
temp (°C)	conv	PT (fan)	PT (nat)	conv	PT (fan)	PT (nat)
40	188 ± 43	208 ± 53	209 ± 48	76.1 ± 0.6	76.3 ± 0.6	75.0 ± 0.7
50	**350 ± 79**	204 ± 39	143 ± 32	**61.2 ± 0.6**	72.6 ± 0.4	76.4 ± 0.5
60	307 ± 76	227 ± 59	202 ± 59	62.9 ± 0.5	**76.8 ± 0.9**	**76.4 ± 0.6**
as fabricated		169 ± 27			77.2 ± 0.4	

[a]All analyzed images are from samples with crystallinity fraction ∼70%. Annealing methods: conv = conventional, PT = photothermal, where fan = fan-cooling and nat = natural cooling. Particular comparisons highlighted in the text are presented in bold font.

tends to preserve morphology; however, annealing times are long. For annealing just below T_m (60 °C), the results are similar to that at 50 °C (Figure 1); that is, the photothermal approaches preserve the nanofiber size and porosity much better than conventional annealing where porosity drops by ∼15% and fiber diameter almost doubles. Note that even when annealing very close to T_m, the sample porosity is almost unchanged for the photothermal modalities. We conclude that for reasonable annealing times, which requires an annealing temperature relatively close to T_m, photothermal heating produces a much more favorable outcome even for the same crystallinity increase—that is, the ability to maintain mat nanofibrous morphology while also altering the interior of the material.

3.2. Increased Maximum Crystallinity with Inhomogeneous Heating. As discussed above, the maximum crystallinity achieved for conventional annealing is ∼71%. However, as summarized in Figure 2, significantly larger values (up to 78%) were observed for photothermal modalities. In this section, we discuss the origin of these results. Examining the effect of temperature within each modality provides information on the distribution of environments within the nanofibers. For the conventional annealing approach, as the annealing temperature changes, the time scale is compressed or expanded (as expected from time–temperature superposition[38] with no, or only a slight, increase in the maximum achievable crystallinity (Figure 2a)). Thinking of the crystallization process as thermally activated where a well-defined barrier must be overcome in order to transition a segment or region from amorphous to crystalline, increasing the temperature should lead to a decrease in the time to maximum crystallinity.

In contrast, for the photothermal modalities, the dominant effect as the average temperature increases is an increase in the maximum crystallinity (Figure 2b,c) with less of or no decrease in the required time. For instance, for either photothermal approach, as the temperature increases from 50 to 60 °C, the speed to maximum crystallinity is not improved, but rather, a much higher crystallinity is achieved. This result is consistent with the presence of a wide range of barriers or multiple distinct and significantly different barrier values. The highest barrier environments are simply inaccessible at lower temperature (i.e., the rate to thermally activate is prohibitively small), which limits the maximum crystallinity achieved and results in the dynamics of the crystallization process being dominated by the lower barrier population. This scenario is consistent with the conventional annealing data, where the decreased time to maximum crystallization is consistent with the change in temperature and a fixed barrier value. However, when much higher temperatures are applied (in this case, for photothermal heating, the temperature at some points in the sample may even exceed the bulk melting point), these higher barriers environ-

ments can be converted, resulting in an increase in the maximum crystallinity. In this case, at elevated temperature the average dynamics will reflect a different distribution of barriers, including larger barrier values, thus reducing the expected increase in apparent crystallization rate.

This interpretation is supported by the presence of an apparent multistage increase in crystallinity under annealing. For instance, examining the effect of annealing at 60 °C (Figure 3), the first stage, which is identical under all modalities,
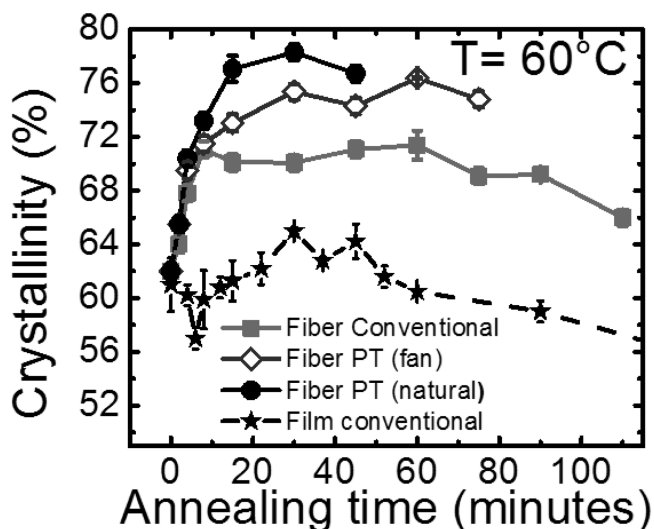

Figure 3. Crystallinity as a function of annealing time in nanofibers (solid lines) as compared to solution crystallized spin-cast films (dotted lines) when annealed at 60 °C by conventional and photothermal (PT) heating. For the nanofibers, all curves overlap at low times, indicating that the increase in crystallinity from 62 to ∼70% is relatively facile. Additional data in the recrystallization region (after the maximum value has been achieved) for the higher temperature data have been removed to ensure readability.

happens rapidly with a sharp increase in crystallinity from 62 to ∼70% over a ca. 8 min annealing period. Then the photothermal samples continue to increase in crystallinity (to a maximum of 75 and 78%) over the next 20–50 min for naturally or fan-cooled samples, respectively. No further increase in crystallinity is observed for the conventionally treated samples after the initial jump, and as at lower annealing temperatures, the maximum crystallinity is ∼70–71% until melting and recrystallization occur. If there is a distribution of environments within the nanofibers, with polymer segments that are easier (low barrier) or more difficult (high barrier) to reorient, the higher temperature near the nanoparticles during photothermal heating may access higher barrier material and thus lead to higher overall crystallinity. Spontaneous

segregation of the nanoparticles (as discussed in section 3.4) may aid in this process. The higher barrier material apparently cannot be crystallized by uniform conventional heating because the energy required for segment reorientation would result in overt melting of other crystallites, resulting in no overall gain in crystallinity fraction. A physical explanation for different barriers in a semicrystalline nanofibrous system could be the presence of row-nucleated structures due to chain elongation in the fiber-forming process where aligned amorphous material is relatively easy to crystallize. We note that for the highest crystallinity samples some loss of nanofibrous morphology can occur. For instance, for the photothermal fan-cooled samples with 76 ± 1% crystallinity, average fiber diameter is 290 ± 90 nm with 52% porosity.

3.3. Crystal Structure.
Wide-angle X-ray diffraction (WAXD) provides information about the crystalline structure within the nanofibers. WAXD revealed two crystalline peaks ($2\theta \sim 19.0°$ (120 reflection) and 23.1° (112 reflection)) as expected for poly(ethylene oxide). As has been previously observed for electrospun samples,[62,63] the 19.0° peak is smaller in amplitude than that at 23.1°. An example of the intensity as a function of 2θ is presented as Supporting Information. As expected, the integral peak area increased with annealing temperature and time, indicative of increased crystallinity. Quantification of the crystallinity from WAXD was not possible due to a convoluted amorphous halo, which was not seen in previous studies on film samples and may be attributed to the roughness of the fibrous mat samples. Crystallite thickness was calculated using the Scherer equation,[61,64] and the results for select samples are shown in Table 2. For both annealing

Table 2. Average Crystal Size and FWHM from WAXD Patterns of As-Spun and Annealed AuNP:PEO Nanofibers at 40 °C (180 min) and 60 °C (30 min)[a]

annealing temp, time	annealing technique	$2\theta \sim 19.01°$	
		av crystal size (Å)	FWHM (deg)
control	n/a	298	0.28
40 °C, 180 min	conv	305	0.27
	PT (fan)	346	0.24
	PT (nat)	391	0.21
60 °C, 30 min	conv	325	0.25
	PT (fan)	356	0.23
	PT (nat)	401	0.21

[a]PT = photothermal annealing; conv = conventional annealing; fan = fan cooling; nat = natural cooling.

conditions studied (40 °C for 180 min and 60 °C for 30 min) the crystallite thickness (120 reflection measured from $2\theta \sim 19.0°$) increased as a function of annealing method (smallest for conventional and largest for natural cool photothermal). This trend is consistent with the increases in crystallinity as shown by the DSC studies discussed above.

3.4. Natural Cooling and Nanoparticle Segregation.
Figures 1−3 show examples of the differences in crystallinity increase comparing the two photothermal modalities: natural cooling and fan-forced cooling. We note that at any given treatment temperature the naturally cooled photothermal samples achieve higher crystallinities at shorter annealing times, which is logical due to the slower cooling rate. To quantify this effect, one approach is to assign an effective annealing time (intentional annealing plus additional cooling

time) for naturally cooled samples—this would shift the "photothermal natural" curves to longer times. For instance, for the 50 °C data, if the effective annealing time is 17 min longer than the intended time, then the data from natural cooling overlaps with that from photothermal heating with fan cooling (Figure 4). Seventeen minutes is the correct order of magnitude difference in time between natural cooling and that for the fan-cooled modality.
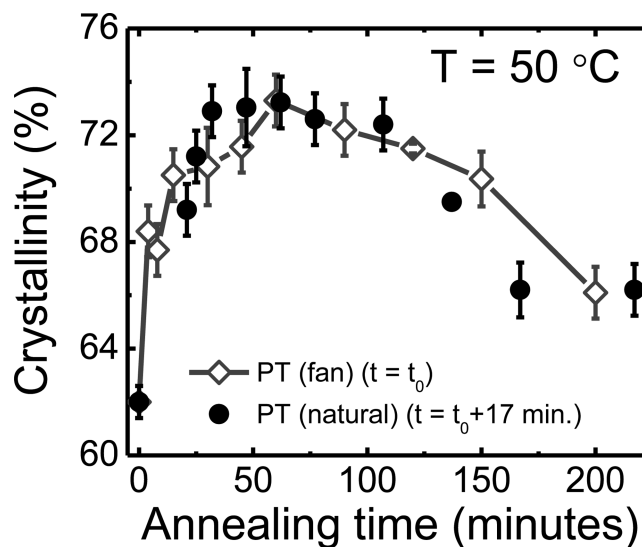

Figure 4. Comparison of the results of photothermal (PT) annealing with fan cooling (open diamond symbols) with the effect of photothermal annealing with natural cooling. The time scale for the natural-cooled modality has been shifted by 17 min to reflect the additional time during which the sample is experiencing elevated temperatures.

However, data from higher and lower temperatures reveal additional information. Examining Figure 2, one observes that while the maximum crystallinity achieved for treatment at 50 °C is similar for the two different photothermal modalities (73−74%), for treatment at both 40 and 60 °C, the maximum crystallinity for photothermal treatment with natural cooling is much higher than that attained under the fan-cooling condition (74 vs 69% and 78 vs 75%, respectively). Thus, no possible shift of the time axis will allow the two curves to match. For instance, examining the results for annealing at 40 °C, the maximum crystallinity achieved via the natural-cooling photo-thermal modality is 74% at 325 min. This result cannot be realized by simply annealing for a longer time and then fan cooling. In fact, the maximum crystallinity attained via annealing with photothermal heating and then fan cooling for any time (4−600 min) is 69%. Furthermore, at early times (<10−15 min) for all temperatures, results from the two different photothermal modalities are almost identical (without any time shifts). The data for annealing at 60 °C (Figure 3) illustrate this well: photothermal treatment of 2 min with a natural cool results in only a modest increase in crystallinity (66% vs 62% before any treatment), identical to the result for 2 min annealing and then application of the fan, even though the natural-cooled sample is warm for much longer (ca. an additional 17 min).

Thus, to summarize, natural cooling does not seem to accelerate the initial fast crystallization process, which can be thought of as involving material with a relatively low barrier to

crystallization, such as might occur in regions with aligned polymeric chains. However, in contrast, the natural cooling appears to particularly target the higher barrier material that is more difficult to crystallize—in fact, in this study, this fraction of the sample could not be crystallized via conventional annealing. Previously we[38] and others[69−73] have argued that nanoparticles (here, 19 nm diameter) are unlikely to be included within crystalline regions in semicrystalline polymers but rather likely reside in the amorphous regions between crystallites (with an average size of ∼28 nm for PEO).[23]

However, within a nanofiber, the amorphous material is also heterogeneous, with regions where chains are significantly aligned due to the fiber-forming process.[74] Such aligned material is likely to be relatively easy to crystallize, as the chains are already elongated and have decreased entanglement and thus may be associated with the lower barrier, fast crystallization process that is observed for all annealing modalities. Sufficiently tight packing of chains may prevent nanoparticle encapsulation within these regions during fiber formation.

Figure 3 compares the results for conventional annealing of nanofibers with those obtained for thin films. The initial crystallization for thin films before any treatment, 61 ± 2%, matches that for nanofibers. However, thin films do not show the fast increase in crystallinity at short times observed for the nanofibers, indicating that the low barrier to crystallinity population is not present within the thin films, consistent with identifying such material regions as elongated and aligned amorphous chains, which are oriented during the fiber-forming process of electrospinning. This observation also indicates that conventional annealing of nanofibers primarily results in crystallization of this relatively aligned amorphous material, with maximum crystallinity being achieved in ∼10 min. In contrast, within thin films, for a conventional anneal at 60 °C, the crystallinity maximizes after treatment of ∼30 min—a much longer time scale, which is similar to the time to maximum crystallization for photothermal heating at the same average temperature. This comparison suggests that the "more difficult to crystallize" material within the nanofibers may be similar to the "regular" amorphous material within thin films.

4. CONCLUSIONS

The ability to transform the interior of a nanosized polymeric object without melting the surface, and thus destroying the nanostructure, is a powerful tool. Here, we have shown that by utilizing photothermal heating, the crystallinity fraction in polymer nanofibers can be manipulated, with total crystallinity values that approach the theoretical maxima for an entangled polymer (∼80%). Photothermal annealing also better preserves nanofibrous morphology. Both the ability to preserve fibrous morphology and achievement of higher crystallinity values due to accessing higher barriers reflect the innate difference in nanoparticle-driven photothermal heating as compared to the conventional heating approach—that the temperature is spatially inhomogeneous. These outcomes are possible because heat is predominantly applied within amorphous material, which provides energy for the amorphous chains to reorient and potentially crystallize but while also preserving the existing crystallites (which are not directly heated and thus are protected from melting). Nanoparticles are spontaneously segregated within amorphous material due to their character-istic size.[23] This serendipitous organization is a distinct advantage of a nanoparticle-based heating approach. For

instance, small light-absorbing molecules can in principle also be utilized to increase optical energy deposition and lead to heating. However, a molecular-sized object is much more likely to be incorporated homogeneously throughout the polymeric system—losing the spatial specificity that is crucial to large increases in crystallinity seen for nanoparticle heating.

■ ASSOCIATED CONTENT

Ⓢ Supporting Information

The Supporting Information is available free of charge on the ACS Publications website at DOI: 10.1021/acs.macro-mol.6b01655.

> WAXD spectra (Figures S1 and S2) for as-spun and annealed AuNP:PEO nanofibers at 40 and 60 °C for 180 and 30 min, respectively, as well as example TEM images of neat AuNPs and a AuNP:PEO nanofiber (Figure S3) (PDF)

■ AUTHOR INFORMATION

Corresponding Authors
*E-mail liclarke@ncsu.edu (L.I.C.).
*E-mail regorga@ncsu.edu (R.E.G.).

ORCID ⓘ
Russell E. Gorga: 0000-0002-4416-9532

Author Contributions
V.V. and S.M. contributed equally.

Notes
The authors declare no competing financial interest.

■ REFERENCES

(1) Saravanan, S.; Nethala, S.; Pattnaik, S.; Tripathi, A.; Moorthi, A.; Selvamurugan, N. Preparation, characterization and antimicrobial activity of a bio-composite scaffold containing chitosan/nano-hydroxyapatite/nano-silver for bone tissue engineering. *Int. J. Biol. Macromol.* **2011**, 49, 188−193.

(2) Jing, X.; Mi, H.; Peng, J.; Peng, X.; Turng, L. Electrospun aligned poly (propylene carbonate) microfibers with chitosan nanofibers as tissue engineering scaffolds. *Carbohydr. Polym.* **2015**, 117, 941−949.

(3) Jordan, A. M.; Viswanath, V.; Kim, S.; Pokorski, J. K.; Korley, L. T. Processing and surface modification of polymer nanofibers for biological scaffolds: a review. *J. Mater. Chem. B* **2016**, 4, 5958−5974.

(4) Sershen, S. R.; Westcott, S. L.; Halas, N. J.; West, J. L. Temperature-sensitive polymer?nanoshell composites for photother-

mally modulated drug delivery. *J. Biomed. Mater. Res.* **2000**, *51*, 293−298.

(5) Sridhar, R.; Lakshminarayanan, R.; Madhaiyan, K.; Barathi, V. A.; Lim, K. H. C.; Ramakrishna, S. Electrosprayed nanoparticles and electrospun nanofibers based on natural materials: applications in tissue regeneration, drug delivery and pharmaceuticals. *Chem. Soc. Rev.* **2015**, *44*, 790−814.

(6) Sawada, I.; Fachrul, R.; Ito, T.; Ohmukai, Y.; Maruyama, T.; Matsuyama, H. Development of a hydrophilic polymer membrane containing silver nanoparticles with both organic antifouling and antibacterial properties. *J. Membr. Sci.* **2012**, *387*, 1−6.

(7) Sinha-Ray, S.; Sinha-Ray, S.; Yarin, A. L.; Pourdeyhimi, B. Application of solution-blown 20−50nm nanofibers in filtration of nanoparticles: The efficient van der Waals collectors. *J. Membr. Sci.* **2015**, *485*, 132−150.

(8) Li, J.; Claude, J.; Norena-Franco, L. E.; Seok, S. I.; Wang, Q. Electrical energy storage in ferroelectric polymer nanocomposites containing surface-functionalized $BaTiO_3$ nanoparticles. *Chem. Mater.* **2008**, *20*, 6304−6306.

(9) Zhang, B.; Kang, F.; Tarascon, J.; Kim, J. Recent advances in electrospun carbon nanofibers and their application in electrochemical energy storage. *Prog. Mater. Sci.* **2016**, *76*, 319−380.

(10) Shabafrooz, V.; Mozafari, M.; Vashaee, D.; Tayebi, L. Electrospun nanofibers: From filtration membranes to highly specialized tissue engineering scaffolds. *J. Nanosci. Nanotechnol.* **2014**, *14*, 522−534.

(11) Zong, X.; Ran, S.; Fang, D.; Hsiao, B.; Chu, B. Control of structure, morphology and property in electrospun poly (glycolide-co-lactide) non-woven membranes via post-draw treatments. *Polymer* **2003**, *44*, 4959−4967.

(12) Zong, X. H.; Kim, K.; Fang, D. F.; Ran, S. F.; Hsiao, B. S.; Chu, B. Structure and process relationship of electrospun bioabsorbable nanofiber membranes. *Polymer* **2002**, *43*, 4403−4412.

(13) Deitzel, J. M.; Kleinmeyer, J. D.; Hirvonen, J. K.; Beck Tan, N. C. Controlled deposition of electrospun poly(ethylene oxide) fibers. *Polymer* **2001**, *42*, 8163−8170.

(14) Ramaswamy, S.; Clarke, L. I.; Gorga, R. E. Morphological, mechanical, and electrical properties as a function of thermal bonding in electrospun nanocomposites. *Polymer* **2011**, *52*, 3183−3189.

(15) Tan, E.; Lim, C. Effects of annealing on the structural and mechanical properties of electrospun polymeric nanofibres RID B-3307−2011. *Nanotechnology* **2006**, *17*, 2649−2654.

(16) You, Y.; Lee, S.; Lee, S.; Park, W. Thermal interfiber bonding of electrospun poly(L-lactic acid) nanofibers. *Mater. Lett.* **2006**, *60*, 1331−1333.

(17) Ravandi, S. A. H.; Sadrjahani, M. Mechanical and structural characterizations of simultaneously aligned and heat treated PAN nanofibers. *J. Appl. Polym. Sci.* **2012**, *124*, 3529−3537.

(18) Leporatti, S.; Gao, C.; Voigt, A.; Donath, E.; Möhwald, H. Shrinking of ultrathin polyelectrolyte multilayer capsules upon annealing: a confocal laser scanning microscopy and scanning force microscopy study. *Eur. Phys. J. E: Soft Matter Biol. Phys.* **2001**, *5*, 13−20.

(19) You, Y.; Lee, S. W.; Lee, S. J.; Park, W. H. Thermal interfiber bonding of electrospun poly (l-lactic acid) nanofibers. *Mater. Lett.* **2006**, *60*, 1331−1333.

(20) Aou, K.; Kang, S.; Hsu, S. L. Morphological study on thermal shrinkage and dimensional stability associated with oriented poly (lactic acid). *Macromolecules* **2005**, *38*, 7730−7735.

(21) Lee, S. J.; Oh, S. H.; Liu, J.; Soker, S.; Atala, A.; Yoo, J. J. The use of thermal treatments to enhance the mechanical properties of electrospun poly (ε-caprolactone) scaffolds. *Biomaterials* **2008**, *29*, 1422−1430.

(22) Bao, J.; Clarke, L. I.; Gorga, R. E. Effect of constrained annealing on the mechanical properties of electrospun poly(ethylene oxide) webs containing multiwalled carbon nanotubes. *J. Polym. Sci., Part B: Polym. Phys.* **2016**, *54*, 787−796.

(23) Huang, C.; Chen, J. Crystallization and chain conformation of semicrystalline and amorphous polymer blends studied by wide-angle and small-angle scattering. *J. Polym. Sci., Part B: Polym. Phys.* **2001**, *39*, 2705−2715.

(24) Maier, S. A.; Atwater, H. A. Plasmonics: Localization and guiding of electromagnetic energy in metal/dielectric structures. *J. Appl. Phys.* **2005**, *98*, 011101.

(25) Link, S.; El-Sayed, M. Shape and size dependence of radiative, non-radiative and photothermal properties of gold nanocrystals. *Int. Rev. Phys. Chem.* **2000**, *19*, 409−453.

(26) Zharov, V.; Lapotko, D. Photothermal imaging of nanoparticles and cells. *IEEE J. Sel. Top. Quantum Electron.* **2005**, *11*, 733−751.

(27) Boyer, D.; Tamarat, P.; Cognet, L.; Orrit, M.; Lounis, B. Imaging single metal nanoparticles in cells by photothermal interference contrast. *Proc. SPIE* **2003**, *4962*, 121−125.

(28) Zharov, V.; Galitovsky, V.; Viegas, M. Photothermal detection of local thermal effects during selective nanophotothermolysis. *Appl. Phys. Lett.* **2003**, *83*, 4897−4899.

(29) Boyer, D.; Tamarat, P.; Maali, A.; Lounis, B.; Orrit, M. Photothermal imaging of nanometer-sized metal particles among scatterers. *Science* **2002**, *297*, 1160−1163.

(30) Lapotko, D. Optical excitation and detection of vapor bubbles around plasmonic nanoparticles. *Opt. Express* **2009**, *17*, 2538−2556.

(31) Harris, N.; Ford, M.; Cortie, M. Optimization of plasmonic heating by gold nanospheres and nanoshells. *J. Phys. Chem. B* **2006**, *110*, 10701−10707.

(32) Sershen, S.; Westcott, S.; West, J.; Halas, N. An opto-mechanical nanoshell−polymer composite. *Appl. Phys. B: Lasers Opt.* **2001**, *73*, 379−381.

(33) Koerner, H.; Price, G.; Pearce, N. A.; Alexander, M.; Vaia, R. A. Remotely actuated polymer nanocomposites - stress-recovery of carbon-nanotube-filled thermoplastic elastomers. *Nat. Mater.* **2004**, *3*, 115−120.

(34) Zhang, H.; Xia, H.; Zhao, Y. Optically triggered and spatially controllable shape-memory polymer-gold nanoparticle composite materials. *J. Mater. Chem.* **2012**, *22*, 845−849.

(35) Hribar, K. C.; Metter, R. B.; Ifkovits, J. L.; Troxler, T.; Burdick, J. A. Light-Induced Temperature Transitions in Biodegradable Polymer and Nanorod Composites. *Small* **2009**, *5*, 1830−1834.

(36) Xu, H.; Xu, J.; Jiang, X.; Zhu, Z.; Rao, J.; Yin, J.; Wu, T.; Liu, H.; Liu, S. Thermosensitive unimolecular micelles surface-decorated with gold nanoparticles of tunable spatial distribution. *Chem. Mater.* **2007**, *19*, 2489−2494.

(37) Abbott, D. B.; Maity, S.; Burkey, M. T.; Gorga, R. E.; Bochinski, J. R.; Clarke, L. I. Blending with Non-responsive Polymers to Incorporate Nanoparticles into Shape-Memory Materials and Enable Photothermal Heating: The Effects of Heterogeneous Temperature Distribution. *Macromol. Chem. Phys.* **2014**, *215*, 2345−2356.

(38) Viswanath, V.; Maity, S.; Bochinski, J. R.; Clarke, L. I.; Gorga, R. E. Thermal Annealing of Polymer Nanocomposites via Photothermal Heating: Effects on Crystallinity and Spherulite Morphology. *Macromolecules* **2013**, *46*, 8596−8607.

(39) Maity, S.; Downen, L. N.; Bochinski, J. R.; Clarke, L. I. Embedded metal nanoparticles as localized heat sources: An alternative processing approach for complex polymeric materials. *Polymer* **2011**, *52*, 1674−1685.

(40) Son, M.; Im, J.; Wang, K.; Oh, S.; Kim, Y.; Yoo, K. Surface plasmon enhanced photoconductance and single electron effects in mesoporous titania nanofibers loaded with gold nanoparticles. *Appl. Phys. Lett.* **2010**, *96*, 023115.

(41) Wang, P.; Zhang, L.; Xia, Y.; Tong, L.; Xu, X.; Ying, Y. Polymer nanofibers embedded with aligned gold nanorods: a new platform for plasmonic studies and optical sensing. *Nano Lett.* **2012**, *12*, 3145−3150.

(42) Maity, S.; Wu, W.; Xu, C.; Tracy, J. B.; Gundogdu, K.; Bochinski, J. R.; Clarke, L. I. Spatial temperature mapping within polymer nanocomposites undergoing ultrafast photothermal heating via gold nanorods. *Nanoscale* **2014**, *6*, 15236−15247.

(43) Link, S.; El-Sayed, M. A. Spectral properties and relaxation dynamics of surface plasmon electronic oscillations in gold and silver nanodots and nanorods. *J. Phys. Chem. B* **1999**, *103*, 8410−8426.

(44) Maity, S.; Kozek, K. A.; Wu, W.; Tracy, J. B.; Bochinski, J. R.; Clarke, L. I. Anisotropic Thermal Processing of Polymer Nanocomposites via the Photothermal Effect of Gold Nanorods. *Part. Part. Syst. Charact.* **2013**, *30*, 193−202.

(45) Richardson, H. H.; Thomas, A. C.; Carlson, M. T.; Kordesch, M. E.; Govorov, A. O. Thermo-optical responses of nanoparticles: Melting of ice and nanocalorimetry approach. *J. Electron. Mater.* **2007**, *36*, 1587−1593.

(46) Govorov, A. O.; Zhang, W.; Skeini, T.; Richardson, H.; Lee, J.; Kotov, N. A. Gold nanoparticle ensembles as heaters and actuators: melting and collective plasmon resonances. *Nanoscale Res. Lett.* **2006**, *1*, 84−90.

(47) Merabia, S.; Shenogin, S.; Joly, L.; Keblinski, P.; Barrat, J. L. Heat transfer from nanoparticles: a corresponding state analysis. *Proc. Natl. Acad. Sci. U. S. A.* **2009**, *106*, 15113−15118.

(48) Link, S.; El-Sayed, M. A. Shape and size dependence of radiative, non-radiative and photothermal properties of gold nanocrystals. *Int. Rev. Phys. Chem.* **2000**, *19*, 409−453.

(49) Baffou, G.; Quidant, R.; Girard, C. Heat generation in plasmonic nanostructures: Influence of morphology. *Appl. Phys. Lett.* **2009**, *94*, 153109.

(50) Baffou, G.; Girard, C.; Quidant, R. Mapping heat origin in plasmonic structures. *Phys. Rev. Lett.* **2010**, *104*, 136805.

(51) Huang, Z.; Zhang, Y.-Z.; Kotaki, M.; Ramakrishna, S. A review on polymer nanofibers by electrospinning and their applications in nanocomposites. *Compos. Sci. Technol.* **2003**, *63*, 2223−2253.

(52) Song, L.; Chen, Y.; Evans, J. W. Measurements of the Thermal Conductivity of Poly (ethylene oxide)-Lithium Salt Electrolytes. *J. Electrochem. Soc.* **1997**, *144*, 3797−3800.

(53) Richardson, H. H.; Hickman, Z. N.; Govorov, A. O.; Thomas, A. C.; Zhang, W.; Kordesch, M. E. Thermooptical properties of gold nanoparticles embedded in ice: characterization of heat generation and melting. *Nano Lett.* **2006**, *6*, 783−788.

(54) FRENS, G. Controlled Nucleation for Regulation of Particle-Size in Monodisperse Gold Suspensions. *Nature, Phys. Sci.* **1973**, *241*, 20−22.

(55) Maity, S.; Bochinski, J. R.; Clarke, L. I. Metal Nanoparticles Acting as Light-Activated Heating Elements within Composite Materials. *Adv. Funct. Mater.* **2012**, *22*, 5259−5270.

(56) Bur, A. J.; Vangel, M. G.; Roth, S. Temperature dependence of fluorescent probes for applications to polymer materials processing. *Appl. Spectrosc.* **2002**, *56*, 174−181.

(57) Bur, A. J.; Roth, S. C.; Spalding, M. A.; Baugh, D. W.; Koppi, K. A.; Buzanowski, W. C. Temperature gradients in the channels of a single-screw extruder. *Polym. Eng. Sci.* **2004**, *44*, 2148−2157.

(58) Maity, S.; Downen, L. N.; Bochinski, J. R.; Clarke, L. I. Embedded metal nanoparticles as localized heat sources: An alternative processing approach for complex polymeric materials. *Polymer* **2011**, *52*, 1674−1685.

(59) Ojha, S. S.; Afshari, M.; Kotek, R.; Gorga, R. E. Morphology of electrospun nylon-6 nanofibers as a function of molecular weight and processing parameters. *J. Appl. Polym. Sci.* **2008**, *108*, 308−319.

(60) Wieczorek, W.; Such, K.; Florjanczyk, Z.; Stevens, J. Polyether, polyacrylamide, LiClO4 composite electrolytes with enhanced conductivity. *J. Phys. Chem.* **1994**, *98*, 6840−6850.

(61) Bortel, E.; Hodorowicz, S.; Lamot, R. Relation between crystallinity degree and stability in solid state of high molecular weight poly (ethylene oxide) s. *Makromol. Chem.* **1979**, *180*, 2491−2498.

(62) Zhang, J.; Yang, D.; Xu, F.; Zhang, Z.; Yin, R.; Nie, J. Electrospun core− shell structure nanofibers from homogeneous solution of poly (ethylene oxide)/chitosan. *Macromolecules* **2009**, *42*, 5278−5284.

(63) Deitzel, J. M.; Kleinmeyer, J.; Harris, D.; Beck Tan, N. C. The effect of processing variables on the morphology of electrospun nanofibers and textiles. *Polymer* **2001**, *42*, 261−272.

(64) Khan, J.; Harton, S. E.; Akcora, P.; Benicewicz, B. C.; Kumar, S. K. Polymer crystallization in nanocomposites: spatial reorganization of nanoparticles. *Macromolecules* **2009**, *42*, 5741−5744.

(65) Wang, B.; Li, B.; Xiong, J.; Li, C. Y. Hierarchically ordered polymer nanofibers via electrospinning and controlled polymer crystallization. *Macromolecules* **2008**, *41*, 9516−9521.

(66) Xu, X.; Wang, H.; Jiang, L.; Wang, X.; Payne, S. A.; Zhu, J.; Li, R. Comparison between cellulose nanocrystal and cellulose nanofibril reinforced poly (ethylene oxide) nanofibers and their novel shish-kebab-like crystalline structures. *Macromolecules* **2014**, *47*, 3409−3416.

(67) Salalha, W.; Dror, Y.; Khalfin, R. L.; Cohen, Y.; Yarin, A. L.; Zussman, E. Single-walled carbon nanotubes embedded in oriented polymeric nanofibers by electrospinning. *Langmuir* **2004**, *20*, 9852−9855.

(68) Acierno, D.; Lavorgna, M.; Piscitelli, F.; Russo, P.; Spena, P. Polyester-based nanocomposite fibers: A preliminary investigation on structure, morphology, and mechanical properties. *Adv. Polym. Technol.* **2011**, *30*, 41−50.

(69) Guidelli, E. J.; Ramos, A. P.; Zaniquelli, M. E. D.; Nicolucci, P.; Baffa, O. Synthesis and characterization of silver/alanine nanocomposites for radiation detection in medical applications: the influence of particle size on the detection properties. *Nanoscale* **2012**, *4*, 2884−2893.

(70) Burgaz, E. Poly (ethylene-oxide)/clay/silica nanocomposites: Morphology and thermomechanical properties. *Polymer* **2011**, *52*, 5118−5126.

(71) El-Zaher, N. A.; Melegy, M. S.; Guirguis, O. W. Thermal and structural analyses of PMMA/TiO 2 nanoparticles composites. *Nat. Sci.* **2014**, *6*, 859−870.

(72) Dorigato, A.; D'Amato, M.; Pegoretti, A. Thermomechanical properties of high density polyethylene−fumed silica nanocomposites: effect of filler surface area and treatment. *J. Polym. Res.* **2012**, *19*, 1−11.

(73) Bernardo, G.; Bucknall, D. G. *Recent Progress in the Understanding and Manipulation of Morphology in Polymer: Fullerene Photovoltaic Cells*; In-Tech Publications: 2012.

(74) Hamlett, C. A.; Jayasinghe, S. N.; Preece, J. A. Electrospinning nanosuspensions loaded with passivated Au nanoparticles. *Tetrahedron* **2008**, *64*, 8476−8483.